Impact of the Electromagnetic Brake Position on the Flow Structure in a Slab Continuous Casting Mold: An Experimental Parameter Study

Schurmann, D.; Glavinic, I.; Willers, B.; Timmel, K.; Eckert, S.;

Originally published:

January 2020

Metallurgical and Materials Transactions B 51(2020)1, 61-78

DOI: https://doi.org/10.1007/s11663-019-01721-x

Metallurgical and Materials Transactions B manuscript No.
(will be inserted by the editor)

Impact of the Electromagnetic Brake Position on the Flow Structure in a Slab Continuous Casting Mold: An Experimental Parameter Study

Dennis Schurmann · Ivan Glavinić · Bernd Willers · Klaus Timmel · Sven Eckert

Received: 27.06.2019 / Accepted: 02.10.2019

Abstract Flow measurements are performed in a slab model for continuous casting of steel under the influence of a ruler type Electromagnetic Brake (EMBr). The Mini-LIMMCAST facility utilizes the low melting GaInSn alloy for flow modeling. Two-dimensional velocity distributions in the center plane of the rectangular mold with a cross-section of $300 \times 35\,\mathrm{mm}^2$ are determined by means of the Ultrasound Doppler Velocimetry (UDV). This study especially focuses on the influence of the vertical position of the EMBr and its magnetic flux density as well as the effect of different immersion depths of the Submerged Entry Nozzle (SEN).

The horizontal flow velocity just below the free surface can effectively be reduced by choosing an optimal position of the EMBr while an improper positioning even increases the near-surface velocity compared to the case without activated brake. A general braking effect of the EMBr on the submerged jet is not observed. The decisive mechanism for controlling the near-surface flow results from a modification of the jet geometry and a reorganization of the flow field. In terms of an effective flow control an appropriate positioning of the EMBr has at least the same significance as the regulation of the magnetic field strength.

Keywords Continuous Slab Casting · Liquid Metal Model Experiments · Flow Measurements · Ultrasound Doppler Velocimetry (UDV) · Electromagnetic Brake (EMBr) · Immersion Depth

Dennis Schurmann · Ivan Glavinic · Bernd Willers · Klaus Timmel · Sven Eckert
Helmholtz-Zentrum Dresden-Rossendorf e.V. (HZDR),
Bautzner Landstraße 400, 01328 Dresden, Germany
E-mail: d.schurmann@hzdr.de

1 Introduction

Electromagnetic Brakes (EMBr) have been widely used in slab continuous casting for many years to improve the quality of the cast product and to increase the productivity of the process. The history of the application of EMBr's in steel casting ranges from the first application of local brakes over level brakes (Single-Ruler-EMBr) towards flow control brakes / molds (Double-Ruler-EMBr). For the local brake, the electromagnetic field is restricted to a confined area close to the jet, while the level brake applies the magnetic field over the whole width of the mold. Finally, the Double-Ruler-EMBr is composed of two level magnetic fields positioned at the free surface and in the jet region, respectively. The variety of possible combinations of different parameters, such as mold geometry, casting speed, immersion depth and geometry of the Submerged Entry Nozzle (SEN) or the type, position and strength of the electromagnetic brake, makes it difficult to find the optimal configuration to achieve the best product quality at the lowest possible cost.

The fluid flow in the mold is considered responsible for most of the casting defects that cause quality problems[10]. Therefore, systematic research into the process continues to be important and relevant to industrial applications today. Recent reviews by Thomas and Cho[3,34] give a very detailed overview of previous research activities with respect to physical modeling and numerical simulations in the field of continuous casting, in particular for influencing the mold flow by means of electromagnetic fields. The numerical simulations, which have developed incomparably in recent decades, play a central role here. Due to increasing computational performance researchers improve their codes in terms of grid resolution and extend them to describe multiphysics by considering many different effects, such as solidification, free surface behavior, two phase flow and flow control by electromagnetic fields. In turn, this means again significant

increases in the computational effort, which is why most published numerical studies are restricted to the investigation of only a few combinations of operating parameters. In addition, the complexity of highly turbulent flow processes in such non-trivial geometries makes any direct numerical simulation impossible for real parameters until today, and instead requires the development of new powerful models that, in turn, must be validated using experimental data.

There has been a number of past work to obtain process data under real production conditions [2,8,15,19]. Unfortunately, due to the harsh operating conditions in the steel casting process, fluid flow measurements in plant trials are mainly restricted to the flow just below the free surface. For this purpose, methods like nail-board measurements [2,15] and the paddle rod technique [8,19,41] are well-established.

Laboratory-scale physical models are another option focusing on measurements in simplified arrangements. Although not all aspects of the process can be considered here, such experiments allow to study particular effects and mechanisms in detail. Appropriate measurement techniques are available that deliver results with a high temporal and spatial resolution. Moreover, these experimental facilities are characterized by a high flexibility which means, for example, that with limited effort, many geometric variations can be realized in a short time. Experimental studies on the fluid flow in the continuous casting process are conducted mainly in large scale water models [14,24,27,32]. However, the effect of electromagnetic actuators (electromagnetic brakes or stirrers) can not be investigated in water models. Therefore, low melting point liquid metal model experiments have been conducted to investigate the fluid flow in continuous casting under the influence of electromagnetic brakes [9,13,28,36,40,42].

Many different EMBr configurations have been considered so far in the previously published literature. For example, Harada et al. [9] studied the effect of both a local and a single-ruler EMBr configuration by numerical simulations and experiments in mercury. The measuring principle of the Vives sensor used here entails a substantial restriction, since such probes cannot provide any values in the EMBr region. The authors observe a lower braking force in the case of the local EMBr and attribute this to the partial coverage of the mold compared to the single-ruler EMBr. Moreover, they suggest that the large recirculating flow below the SEN is transformed into a plug-like flow in vertical direction by the single-ruler EMBr. The authors observed an influence of the EMBr on the fluid velocities below the meniscus, whereas the application of medium magnetic flux densities results in an increase of the near-surface flow.

Moon et al. [25] reported about plant trials using two different types of single-ruler EMBr's at two positions, directly at the nozzle ports and just below the SEN. The higher EMBr position caused perturbations at the surface leading to a deterioration of the internal quality of the slab, while a lower amount of sub-surface defects and inner inclusions were found for the lower EMBr position. Hwang et al. [12] tried to find an explanation for these results by means of corresponding numerical simulations. The authors suggest that at high magnetic field strengths it is difficult for the jet to penetrate into the magnetic field region. In the consequence, a kind of channelling effect or the formation of bypass flows occur which are assumed to be the reason for the negative effect of the EMBr.

Haiqi et al. [7] conducted numerical calculations of the mold flow for four different positions of a local EMBr with a large pole face area covering the main part of the jet. The velocity plots in this work show a reduction of the jet zone by an increasing magnetic field, but do not reveal a distinct modification of the flow structure due to a shift of the EMBr location. Nevertheless, it was found that the higher the brake is positioned, the lower are the velocities near the surface.

Garcia-Hernandez et al. [6] published another numerical study on the influence of a single-ruler EMBr on the mold flow in a slab caster. The authors considered a few variations of the magnetic flux density for two different EMBr positions centering the field domain either across or just below the nozzle ports. A single-roll flow structure was found in the lower part of the mold if the electromagnetic brake was positioned at the SEN ports while an EMBr position below the SEN causes a plug-like flow in vertical direction. It was also observed that the jet was shifted upward with increasing magnetic field strength. The velocities below the meniscus are fastest in the corners of the mold. This maximum moves toward the SEN with increasing magnetic flux density. Lower surface velocities occur for the case of the higher EMBr position.

Experimental studies in GaInSn using a single-ruler EMBr installed at the same height as the nozzle ports were conducted by Timmel et al. [36]. Flow measurements by means of the Ultrasound Doppler Velocimetry (UDV) show that the application of the magnetic field reduces both the penetration depth of the jet and the impinging velocity onto the narrow side wall. The jet was deflected upward with increasing strength of the EMBr. An important outcome is the observation that the application of the magnetic field does not necessarily result in a braking of the flow. Under certain conditions the EMBr may even produce intense fluctuations associated with non-steady and non-isotropic flow structures. The flow structure becomes almost two-dimensional. Furthermore, it was shown that the effect of the EMBr also strongly depends on the wall conductivity. These experimental data was used by several authors to validate numerical simulations [1,22,23,31,35]. On the other hand, the data from [36] are of limited use in terms of brake optimization because only one EMBr position is taken into account and fluid velocities were not measured directly at the surface.

A continuation of this work was reported by Thomas et al.[35]. Numerical and experimental data were obtained for two cases of an single-ruler EMBr, the positioning of which is very similar to the configurations used in[6]. In contrast to[6], the numerical results show lower surface velocities for the deeper EMBr position. Unfortunately, the numerical simulation in[35] does not contain a comparison with respect to the case without magnetic field.

The sum of all previously found results shows quite clearly that the impact of an electromagnetic brake on the flow in the mold is quite complex, and is not limited to a straightforward braking effect. In view of the sometimes contradictory statements of some numerical studies, further experimental investigations are of great importance. However, we are not yet aware of a consistent systematic study that more closely examined the effect of an EMBr on the mold flow based on finely graded variations in key parameters such as magnetic field strength, brake position, or immersion depth of the SEN. The achievement of outstanding product qualities, however, depends in a particular way on whether it is possible to identify an optimal combination of these parameters. The present study should contribute to fill this knowledge gap. This paper focuses on the influence of the above mentioned parameters on the flow distribution in a slab casting mold, especially on the velocities below the meniscus. For that purpose, a comprehensive experimental study was performed using the mockup facility Mini-LIMMCAST filled with the low melting point metal alloy GaInSn. Details of the experimental setup and the measuring technique applied are given in Section 2. The results of the flow measurements are presented in Section 3 and discussed in Section 4. The output of this study is concluded in Section 5.

2 Experimental Setup

2.1 Mini-LIMMCAST Facility

All experiments within this study are carried out in the Mini-LIMMCAST facility at HZDR, a cold liquid metal loop to model the fluid flow in the continuous casting process of steel[37,38]. This setup uses GaInSn as a model fluid which has thermo-physical properties close to those of liquid steel (cf. Table 1). The eutectic composition of this alloy is liquid at room temperature. All measurements are performed under isothermal conditions at room temperature.

The liquid metal is continuously pumped from a reservoir to the tundish. A stopper rod controls the liquid flow rate through the SEN into the mold. The pump is regulated in such a way that the liquid level in the tundish is kept constant throughout the experiments. The loop is closed via a dam, which determines the level in the mold, back to the reservoir.

The experiments presented in this study are conducted in a continuous operation mode, allowing long measurement campaigns with developed flow conditions. At the beginning of each experiment, the stopper rod is maximally opened to achieve a complete filling of the SEN, before the stopper rod position is set to a value of 5 mm. This corresponds to a maximum velocity in the SEN of $v_{SEN,max} \approx 1.0\,\mathrm{m/s}$. The latter has been measured by a single UDV transducer attached under an angle of 30 deg to the SEN.

Table 2 lists the main dimensions and parameters of this study and Figure 1 shows the schematic view of the slab mold and the SEN, both made of PMMA. The model of the mold (Figure 1(a)) has a cross-section of $300 \times 35\,\mathrm{mm}^2$ and a length of 600 mm. Compared to the slab mold setup used in previous studies[23,36], the width of the mold is increased from 140 mm to 300 mm. The new setup provides a larger distance before the jet impinges at the wall. The submerged entry nozzle (Figure 1(b)) has an inner diameter of 12 mm and rectangular ports, aligned 15 deg downward.

The origin of the Cartesian coordinate system is placed at the position of the free surface on the central axis of the mold. The velocity vector $\mathbf{v}$ is composed of the velocity components u, v and w, which are positive when they are oriented in the direction of the coordinate axes, $\mathbf{e_x}$, $\mathbf{e_y}$ and $\mathbf{e_z}$, respectively:

$$\mathbf{v} = u\,\mathbf{e_x} + v\,\mathbf{e_y} + w\,\mathbf{e_z} \tag{1}$$

2.2 Electromagnetic Brake

The electromagnetic brake is capable to generate a magnetic flux density of up to $B = 404\,\mathrm{mT}$ in its center. Two coils, positioned on each side of the mold, are connected in series to a constant current source with a current of up to $I_{max} = 600\,\mathrm{A}$. Each coil consists of $N_c = 32$ windings, resulting in a total of up to $N_c I_{max} = 19\,200\,\mathrm{A}$ turns. The height position of the electromagnetic brake at the mold can be adjusted easily using a motor-driven traversing system. This system allows a positioning of the magnet with a tolerance of about ± 0.5 mm. The variable z_{brake} denotes the distance from the center of the brake to the free surface. When the brake is deactivated ($I = 0$), a remaining magnetic flux density of 6 mT has been measured. This value can be explained by the residual magnetism in the iron core of the magnet system. The potential influence of the residual magnetic field on the flow in the mold is considered in Section 3.1.

Figure 2 shows the measured distribution of the magnetic flux density along the center axes of the brake (x_b, y_b and z_b) for an electric current of $I = 375\,\mathrm{A}$. In the center of the brake the magnetic flux density is $B = 305\,\mathrm{mT}$. Because the extension of the pole pieces of 410 mm exceeds the width of the mold by more than one third, the magnetic flux density at the narrow walls of the mold is still around 98.5 % of the center value. In the vertical direction, the magnetic flux density decays to 90 % at the pole shoe edges and to 50 % in a distance of about 50 mm from the center plane of the brake.

Table 1 Physical properties of liquid steel[11,16,17,21], GaInSn[29] and water[39].

			Liquid Steel	GaInSn	Water
Reference Temperature	T	°C	~ 1500	20	20
Density	ρ	kg/m^3	~ 7000	6353	988
Dynamic Viscosity	η	mPa s	$\sim 2 \ldots 18$	2.18	1.00
Kinematic Viscosity	ν	m^2/s	$\sim 2.86 \times 10^{-7} \ldots 25.7 \times 10^{-7}$	3.44×10^{-7}	10.0×10^{-7}
Electrical Conductivity	σ	1/(Ω m)	$\sim 0.833 \times 10^6$	3.29×10^6	< 50
Thermal Conductivity	λ	W/(m K)	~ 30	23.98	0.598
Surface Tension	γ	N/m	~ 1.7	0.587	7.28×10^{-2}

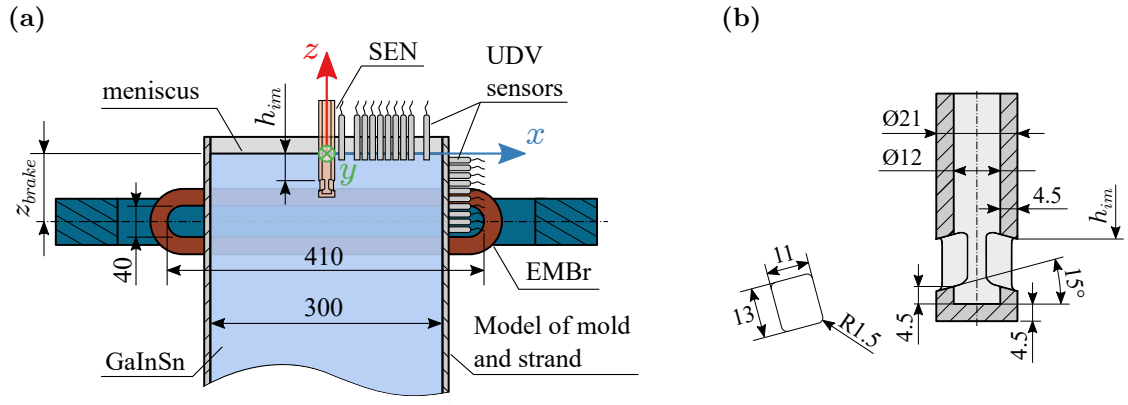

Fig. 1 (a) Schematic view of the main setup (mold, SEN, EMBr and UDV sensors) and (b) cut view of the SEN used in this study. The rectangular port is aligned 15 deg downward.

2.3 Measurement Technique

In this study, the Ultrasound Doppler Velocimetry (UDV) is applied to determine the velocity field in the mold, since it allows accurate measurements with less than 5 % error and is applicable to opaque media such as liquid metals.[4,33]

Table 2 Main dimensions and parameters of the setup.

Mold			
Width	W_m	mm	300
Thickness	T_m	mm	35
Height	H_m	mm	600
Submerged Entry Nozzle			
Immersion Depth	h_{im}	mm	35 ± 10
Inner Diameter	d_i	mm	12
Outer Diameter	d_o	mm	21
Port Width	w_p	mm	11
Port Height	h_p	mm	13
Port Angle	α_p	deg	-15
Max. Velocity	$v_{SEN,max}$	m/s	1.0
Electromagnetic Brake			
Windings per Coil	N_c	-	32
Max. Current	I_{max}	A	600
Max. Mag. Flux Density	B_{max}	mT	404

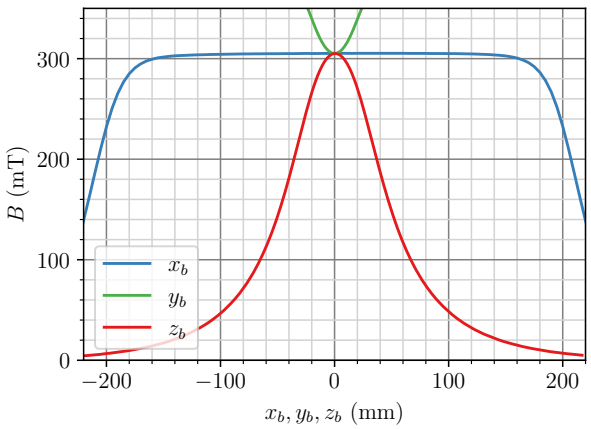

Fig. 2 Measured magnetic flux density B of the brake along its center axes x_b, y_b and z_b for an electric current of $I = 375$ A.

Horizontal and vertical velocity components (u and w) are measured in the mold center plane ($y = 0$). The vertical velocity component w is recorded by several UDV transducers in direct contact with the liquid metal through the free surface. For the measurement of the horizontal velocities, the UDV transducers are placed at the outside of the

8 mm thick PMMA mold wall. The sound speed in PMMA ($c \approx 2750\,\mathrm{m/s}$)[5] is very similar to that in GaInSn ($c = 2730\,\mathrm{m/s}$)[26], which is why diffraction of the ultrasound beam can be neglected. However, the ultrasonic impedance differs due to the gap in the densities ($\rho_{PMMA} = 1190\,\mathrm{kg/m^3}$ compared to $\rho_{GaInSn} = 6353\,\mathrm{kg/m^3}$)[5,29], which is why the ultrasound is reflected at the interface between GaInSn and PMMA to some extent. This wall reflection together with the near-field characteristics of the ultrasound beam results in high ultrasound echo amplitudes for the first few millimeters after the mold wall. This is the reason, why the horizontal velocities for $x > 135\,\mathrm{mm}$, e.g. in a close distance up to 15 mm from the wall, can not be measured. The pulse repetition time t_{pr} has to be chosen properly in order to prevent multiple standing echos arising from the back wall of the mold. Their appearance in the region of interest prevents the measurement of velocities at these locations. To avoid this, t_{pr} is chosen as a multiple of the time t_m, which corresponds to the travel time of the ultrasound burst through the mold.

The divergence of the ultrasonic beam is another important sensor parameter to be considered for the measurements. The radial dimension of the measuring volume increases with increasing distance from the transducer. Taking into account the half opening angle of $\gamma_{-3\,\mathrm{dB}} = 2.9\,\mathrm{deg}$ in GaInSn[18], the radial dimension of the measuring volume in a distance of 100 mm from the transducer is about 7.6 mm. The spatial resolution of about 4 mm in axial direction is determined by the length of the pulse train. Due to oversampling, the distance between neighboring measurement gates is less than 1 mm.

The measurement instrument DOP 3010 (Signal Processing S.A.[30]) is employed within this study. UDV transducers with a piezo diameter of $d_{US} = 5\,\mathrm{mm}$ and a emitting frequency of $f_e = 4\,\mathrm{MHz}$ are chosen. They are arranged in form of a linear array of ten transducers with a spacing of at least 10 mm between the sensors. The transducers are sequentially activated and each sends a short wave train. The sending cycle is repeated several times. Microparticles distributed in the liquid cause echo signals which are received by the same transducer. Combining measurements of the time of flight and the time shift between subsequent echo signals allows for a reconstruction of linear velocity profiles along the propagation direction of the ultrasound (see[4,30] for more details). The linear arrangement of the ten transducers and a stepwise displacement of this sensor array along the narrow side of the mold provides a two dimensional representation of the time-averaged flow field in the $y = 0$ plane of the whole mold.

2.4 Dimensionless Parameters

The dimensionless parameters play a decisive role in the transfer of the results from physical models to real casting plants. They take into account differences in material, geometry and process variables between the model and the real process. In the case considered here the most important fluid-dynamic parameters are the Reynolds number Re and the Froude number Fr or the Hartmann number Ha and the magnetic interaction parameter N for the magnetohydrodynamics. These numbers are defined as follows:

$$Re = \frac{vL}{\nu} \tag{2}$$

$$Fr = \frac{v}{\sqrt{gL}} \tag{3}$$

$$Ha = \sqrt{\frac{\sigma}{\rho\nu}}BL \tag{4}$$

$$N = \frac{Ha^2}{Re} = \frac{\sigma B^2 L}{\rho v} \tag{5}$$

The fluid properties density, dynamic viscosity and electrical conductivity are represented by the symbols ρ, ν and σ, while L, v and B denote the characteristic length scale, the characteristic velocity and the magnetic flux density.

A comparison between model and real application can be performed in a simple manner by introducing appropriate scale factors M_χ as the ratio between the value of a respective quantity in the real (steel) system χ_{steel} and that of the GaInSn model χ_{GaInSn}:

$$M_\chi = \frac{\chi_{steel}}{\chi_{GaInSn}} \tag{6}$$

Based on the size of the Mini-LIMMCAST test section, Table 3 presents the respective dimensions of mold and SEN for scalings from 1:2 to 1:6. Moreover, the table contains the resulting scale factors M_v and M_B for v and B respectively, to fulfill similarity ($M_\chi = 1$) in terms of the dimensionless parameters Re, Fr and Ha, which result from the corresponding variations of the characteristic length L.

These values demonstrate the following issues:

- Assuming that the same flow velocity as in the real plant is realized in the model, the Reynolds similarity can be achieved using a 1:4 model. It is not expedient to aim for a full-scale 1:1 model. A 1:2 model matches the flow conditions if the velocities in the model are smaller by a factor of about two, while in a 1:6 model the velocities have to be about 45% higher.
- In a smaller model, no Froude similarity is achieved at the same flow velocities. This can be compensated by increasing the velocity by a factor of $\sqrt{2}$ (1:2 model) or a factor of $\sqrt{6}$ (1:6 model).
- If all size relations within a geometry are preserved, Re- and Fr-similarity can not be achieved simultaneously.

Table 3 Some geometric values of corresponding real casters at different geometric scales and the necessary scale factors for velocities v and magnetic flux density B to achieve similarity according to Re, Fr and Ha numbers.

		Scale				
		1:2	1:3	1:4	1:5	1:6
Mold						
W_m	mm	600	900	1200	1500	1800
T_m	mm	70	105	140	175	210
Submerged Entry Nozzle						
h_{im}	mm	70	105	140	175	210
d_i	mm	24	36	48	60	72
For Re similarity						
M_v	-	2.08	1.39	1.04	0.83	0.69
For Fr similarity						
M_v	-	0.71	0.58	0.50	0.45	0.41
For Ha similarity						
M_B	-	2.13	1.42	1.06	0.85	0.71

– Hartmann similarity is guaranteed by corresponding modifications of the magnetic flux density as shown in Table 3. The magnet system is readily able to generate the required magnetic fields.

3 Results

3.1 Flow Distribution in the Mold

The two-dimensional flow pattern in the mold was reconstructed by combining time-averaged measurements of the horizontal and vertical velocity components (u and w). A velocity vector composed of both velocity components can be calculated at the points where horizontal and vertical measurement lines intersect. In all contour plots of the velocity fields in this paper, the areas, that are not accessible to the sensors or where no velocity values are available due to the technical conditions described in Section 2.3, have been left white. Figure 3 shows the time-averaged velocity distribution in one half of the mold when the magnetic field is switched off and the immersion depth of the SEN is $h_{im} = 35\,\mathrm{mm}$. Strictly speaking, the magnetic field in case of the deactivated EMBr is not identical to zero. The residual magnetism of the iron core of the magnet system is responsible for an irreducible magnetic flux density of 6 mT as described in Section 2.2. The magnetic interaction parameter N can be used to estimate whether this weak field has an effect on the flow in the mold. Assuming a discharge velocity of the jet of about $0.2\,\mathrm{m/s}$, the calculation returns a very small value of $N \approx 3.3 \times 10^{-3} \ll 1$, which clearly proves that any influence of this residual magnetic field on the flow is negligible.

The pattern of the horizontal velocity component u is displayed in Figure 3(a). The highest horizontal velocities occur in the upper part of the mold for $z \geq -100\,\mathrm{mm}$. Here, the jet leaves the submerged nozzle port with a high positive horizontal velocity component u and moves towards the narrow face of the mold. The occurrence of negative horizontal velocities in the domain between the meniscus and the jet as well as in the deeper region of the mold below $z < -250\,\mathrm{mm}$ indicate the existence of the double-roll flow pattern. The lower roll has a much larger expansion but shows lower flow velocities.

The vertical velocity component w is depicted in Figure 3(b). Due to the near-field characteristic of the ultrasound beam, the velocities near the transducer ($z > -15\,\mathrm{mm}$) are not accessible to a measurement. The contour plot shows four contiguous areas delimited by a sign change of the vertical velocity component. The detection of negative (downward) velocities just below the nozzle and in the upper right corner of the plot, combined with an upward flow in the other two domains, confirms the above-mentioned assumption of the double-roll flow structure. The jet is also clearly visible here. Its exit angle is about $-30\,\mathrm{deg}$ with respect to the narrow wall and the impact point on the side wall is found at $z \approx -85\,\mathrm{mm}$. Here, the vertical flow divides into an upward and a downward component along the wall driving the double-roll together with the suction effect occurring directly above and below the jet.

Figure 3(c) finally depicts the area where horizontal and vertical measurement lines intersect, enabling the reconstruction of a vector field. In this drawing the colors represent the absolute value of the two-dimensional velocity vector $\mathbf{v}$. The highest absolute velocities are measured, where the jet leaves the nozzle port. With growing distance from the nozzle port, the velocity declines and the angle of the jet becomes almost horizontal at $x = 100\,\mathrm{mm}$, $z = -77\,\mathrm{mm}$. After that point, the jet is directed slightly upward and forms the upper circulation roll, while another part flows downward along the narrow wall. As can already be seen in Figures 3 (a) and (b), the lower roll is extended very far into the mold and closes outside the measuring domain ($z < -300\,\mathrm{mm}$).

In the following we will focus on the velocity distribution in the upper part of the mold, where the jet enters the mold. The measurements have shown that all significant changes in the flow field occur in this zone for the parameter range considered here.

3.2 Influence of the EMBr Position

This section considers the effect of different vertical positions of the electromagnetic brake z_{brake} and the magnetic flux density B on the flow field and especially on the horizontal velocities directly under the meniscus. The immersion depth of the nozzle is left constant at $h_{im} = 35\,\mathrm{mm}$. The sensor for

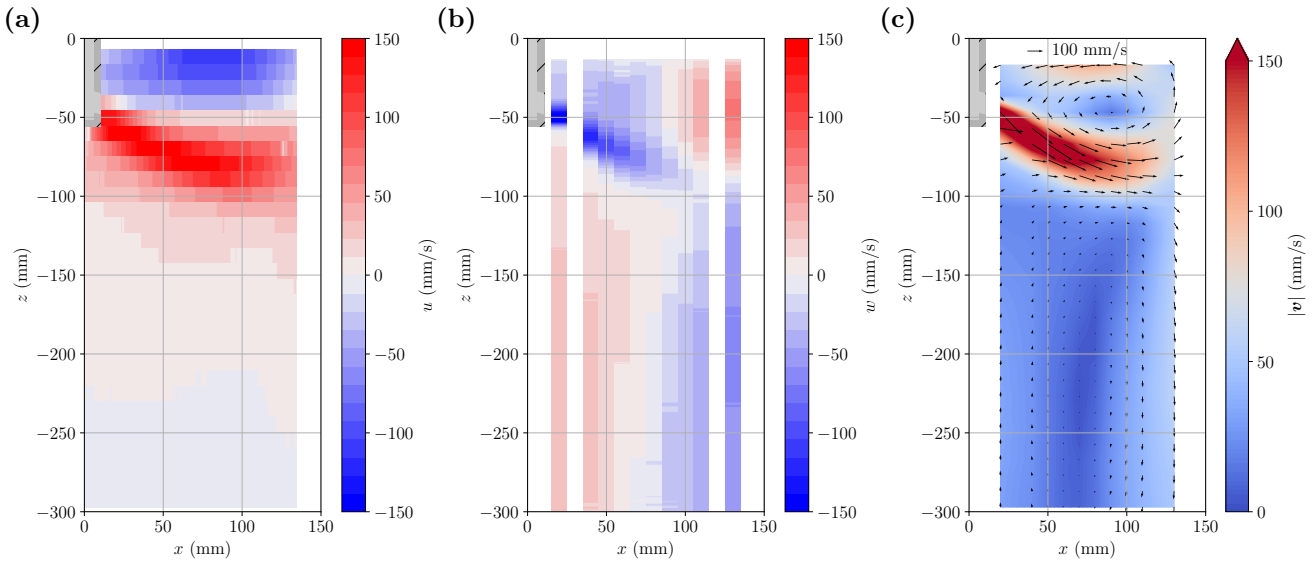

Fig. 3 Contour plots of the time-averaged velocity distribution in the mold measured for the case with deactivated EMBr and an immersion depth of $h_{im} = 35\,\text{mm}$. The colors of the contour plot represent (a) the horizontal velocity component, measured at 30 measurement lines, (b) the vertical velocity component obtained at 10 measurement lines and (c) the absolute velocity at the intersection of the measurement lines. Arrows indicate the two-dimensional velocity at the crossing points of the measurements (a) and (b).

measuring the horizontal velocity with the smallest distance to the free surface is positioned at the height $z = -7\,\text{mm}$.

Figure 4 shows the profiles of the horizontal velocity u along this measuring line close to the free surface for various magnetic flux densities and two exemplary positions of the EMBr. The reason why these particular positions are shown here will become apparent in the following. The symbols indicate the maximum of the absolute velocity $|u|_{max}$.

Figure 4(a) presents the measurements for a relatively low EMBr position at $z_{brake} = -127\,\text{mm}$. All profiles show negative velocity values corresponding to a flow from the side wall towards the SEN with a maximum of $|u|$ occurring in a narrow area approximately between $75\,\text{mm} < x < 85\,\text{mm}$. It becomes obvious, that the application of the EMBr causes an increasing surface velocity with increasing magnetic field strength. The maximum measured velocity is found for $B = 261\,\text{mT}$. The shape of the profiles is preserved with a slight shift of the highest velocity towards the side wall.

The consequence of the magnetic field application on the flow field is different if the EMBr is shifted to a higher position at $z_{brake} = -77\,\text{mm}$, which is just below the SEN (Figure 4(b)). Here, an increase of the near-surface velocities is observed only for small magnetic fields ($B = 53\,\text{mT}$ and $102\,\text{mT}$). Higher magnetic flux densities reduce the horizontal flow below the meniscus significantly. The slowest velocities are observed for $B = 261\,\text{mT}$. A further increase in B modifies the shape of the velocity profiles. The velocity in the center of the mold rises slightly, whereas near the SEN positive velocities occur which indicates a flow from the SEN towards the sidewall.

The next step is to find out if there is a position of the EMBr at which a maximum braking action on the submeniscus velocities can be achieved. For this, the vertical position of the EMBr z_{brake} is varied in small steps for three different magnetic field strengths. $|u|_{max}$, the maximum along x of the time-averaged horizontal velocity profiles recorded at $z = -7\,\text{mm}$, is extracted from the velocity profiles and shown in Figure 5. Here, the blue line marks an averaged value of $110\,\text{mm/s}$ for the case of the deactivated brake, obtained from several measurements at different positions z_{brake}. As was to be expected from the estimates in the previous section, there is no indication that the measured values depend on the brake position. The slight deviations of the individual measured values remain within the measurement uncertainty.

The three curves obtained for different field intensities of the activated EMBr reveal a similar behavior. Compared to the situation without a magnetic field, the near-surface flow is reduced for positioning the brake directly on the free surface with $z_{brake} > -10\,\text{mm}$. When the EMBr position is lowered, the intensity of the flow initially increases and exceeds the value for the deactivated brake. Thereafter, a damping of the near-surface flow occurs, but the extent of which depends on the magnetic field strength. In the case of a magnetic field of $B = 102\,\text{mT}$, the maximum velocity does not fall below of that for the deactivated EMBr at any point. On the other hand, if an EMBr is installed at positions between roughly $-60\,\text{mm}$ and $-90\,\text{mm}$ and generates a magnetic field of $209\,\text{mT}$ or $305\,\text{mT}$, the value without the applied magnetic field can be roughly halved. If the brake position is shifted further down, the velocities near the surface increase again regardless

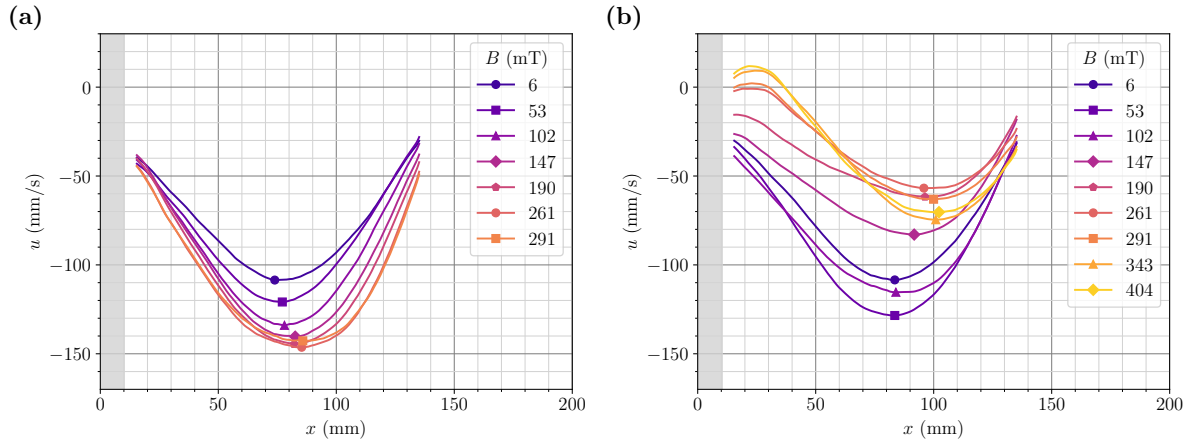

Fig. 4 Time-averaged horizontal velocity u, measured at $z = -7$ mm, for different magnetic flux densities B of the EMBr. The position of the SEN is indicated by a gray shade. The symbols indicate the maximum of the absolute velocity $|u|_{max}$. The brake is positioned at (a) $z_{brake} = -127$ mm and (b) $z_{brake} = -77$ mm.

of which field strength is set. The impact of the magnetic field on the surface flow becomes negligible for $z_{brake} < -200$ mm. Thus, in the configuration considered here, the optimal EMBr position to achieve a maximum braking effect on the velocities below the meniscus is found at around $z_{brake} = -77$ mm, while velocities are increased for a brake position around $z_{brake} = -127$ mm.

Figure 6 presents the evolution of the maximum value of the near-surface horizontal velocity component along x as a function of the magnetic flux density B for the optimal position $z_{brake} = -77$ mm and the deeper position $z_{brake} = -127$ mm. At the lower position, the velocity under the free surface increases gradually with increasing B. A braking effect is not achieved, regardless of which magnetic field

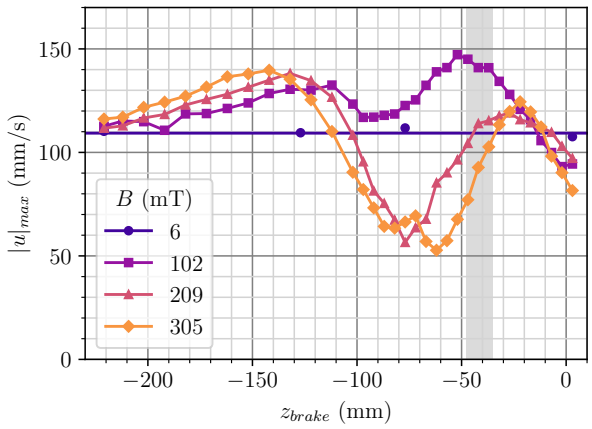

Fig. 5 Maximum along x of the time-averaged horizontal velocity $|u|_{max}$, measured at $z = -7$ mm, with different positions z_{brake} and magnetic flux densities B of the EMBr. The position of the SEN port is indicated by a gray shade.

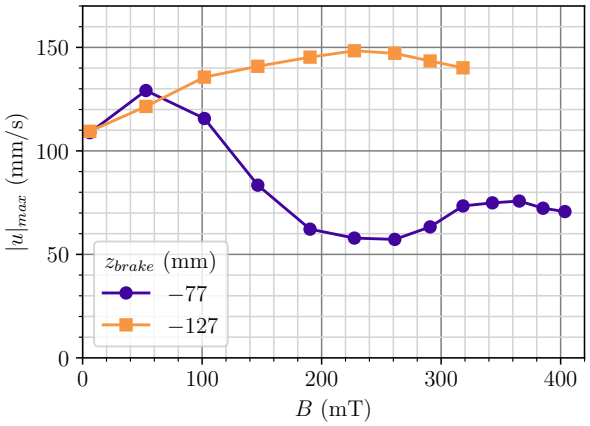

Fig. 6 Maximum along x of the time-averaged horizontal velocity $|u|_{max}$, measured at $z = -7$ mm, with the brake positioned at $z_{brake} = -77$ mm and -127 mm with different magnetic flux densities B.

strength is selected. When the brake is positioned at $z_{brake} = -77$ mm, the velocity rises to 130 mm/s at a low magnetic flux density of $B = 53$ mT. An increase in B leads then to a significant decrease with a minimum of $|u|_{max} \approx 60$ mm/s between 190 mT and 291 mT. For higher magnetic flux densities, the velocity under the free surface increases slightly up to values of around 75 mm/s.

To better understand this behavior, we will now take a closer look at the flow structures. Figure 7 presents selected time-averaged vector plots of the two-dimensional velocity distribution in the upper part of the mold for a brake position of $z_{brake} = -77$ mm and diverse magnetic flux densities B. In the reference case, where the brake is turned off (Figure 7(a)), the jet enters the mold under an angle of about -30 deg. As the distance from the nozzle port increases, the jet directs

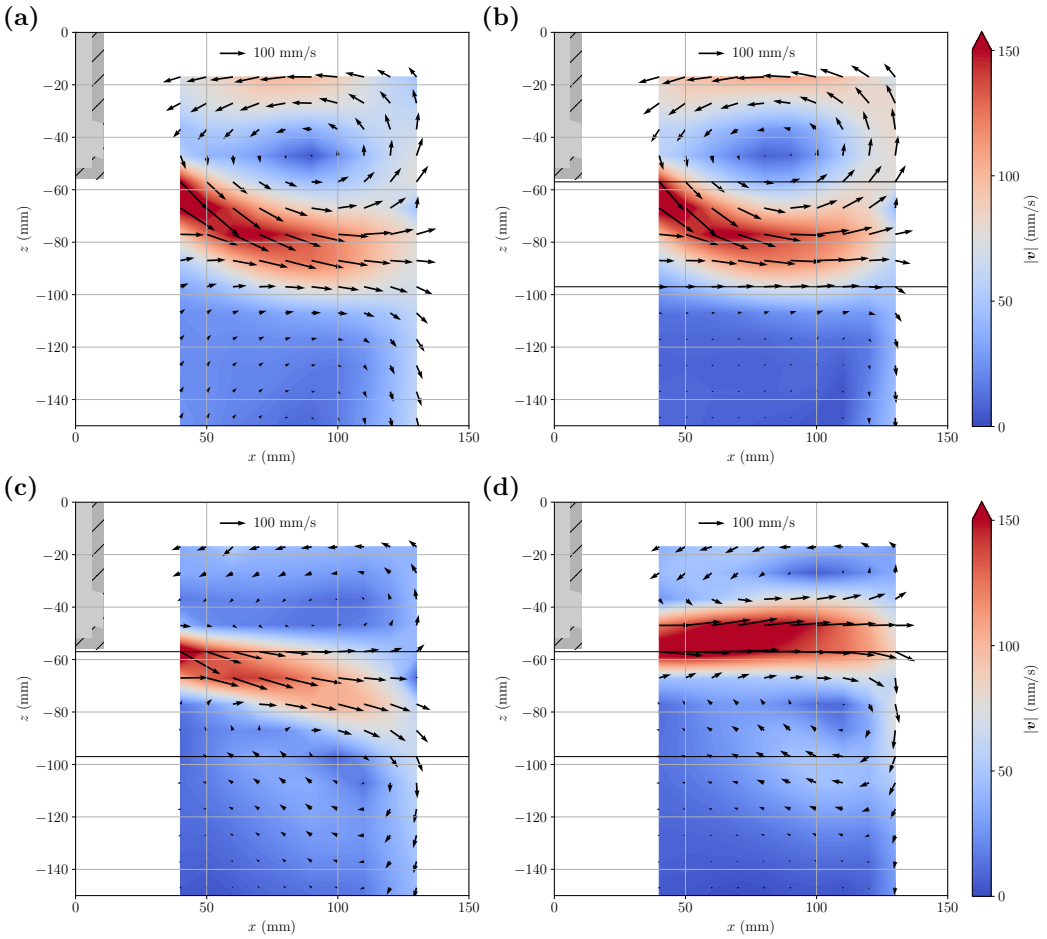

Fig. 7 Vector and contour plot of the time-averaged velocity distribution in the top part of the mold, measured for different magnetic flux densities B (a) EMBr off, (b) 53 mT, (c) 227 mT, (d) 404 mT of the EMBr. The brake is positioned at $z_{brake} = -77$ mm, the edges of the activated EMBr pole shoe are marked by horizontal black lines.

upward and splits into the upper and lower roll before it impinges on the side wall.

When the electromagnetic brake is operated at a low intensity ($B = 53$ mT, Figure 7(b)), the curvature of the jet increases considerably. Its shape resembles that of a banana. This also means that significantly more fluid flows into the upper vortex and therefore intensifies the upper circulation and the near-surface flow. By contrast, the circulation in the lower roll almost vanishes.

Figure 7(c) shows the flow pattern in the mold for the magnetic flux density of 227 mT at which the lowest velocities are observed below the free surface. In this case, a fairly straight shape of the jet is found which runs through the area of the EMBr pole-shoe and is mainly deflected downwards when impinging the wall. A concentrated circulation roll underneath the jet is observed which does not reach the center of the mold. The increase in circulation in the lower roll is associated with a decay in the upper roll, which in turn results in lower velocities below the free surface.

As the intensity of the electromagnetic brake continues to increase ($B = 404$ mT, Figure 7(d)), the jet runs almost horizontally. It is literally pushed out of the region of the brake. Due to the straight exit of the jet, the vertical extent of the upper roll is reduced. This circumstance as well as the fact that the flow intensities in both circulation rolls reach the same level due to the approximately uniform splitting of the jet, might be the reason why the velocities under the free surface slightly increase compared to the previous situation shown in Figure 7(c).

When considering the lower brake position ($z_{brake} = -127$ mm) as shown in Figure 8 it is evident that the shape of the jet is affected much less by the magnetic field strength than in the case of the optimal brake position. The jet keeps its "banana"-like shape for all magnetic flux densities applied and its location is moved only slightly upward by an increase in magnetic flux density. Nevertheless, this small change is sufficient to achieve a similar state as in Figure 7(b)), where the bottom roll almost completely disappears.

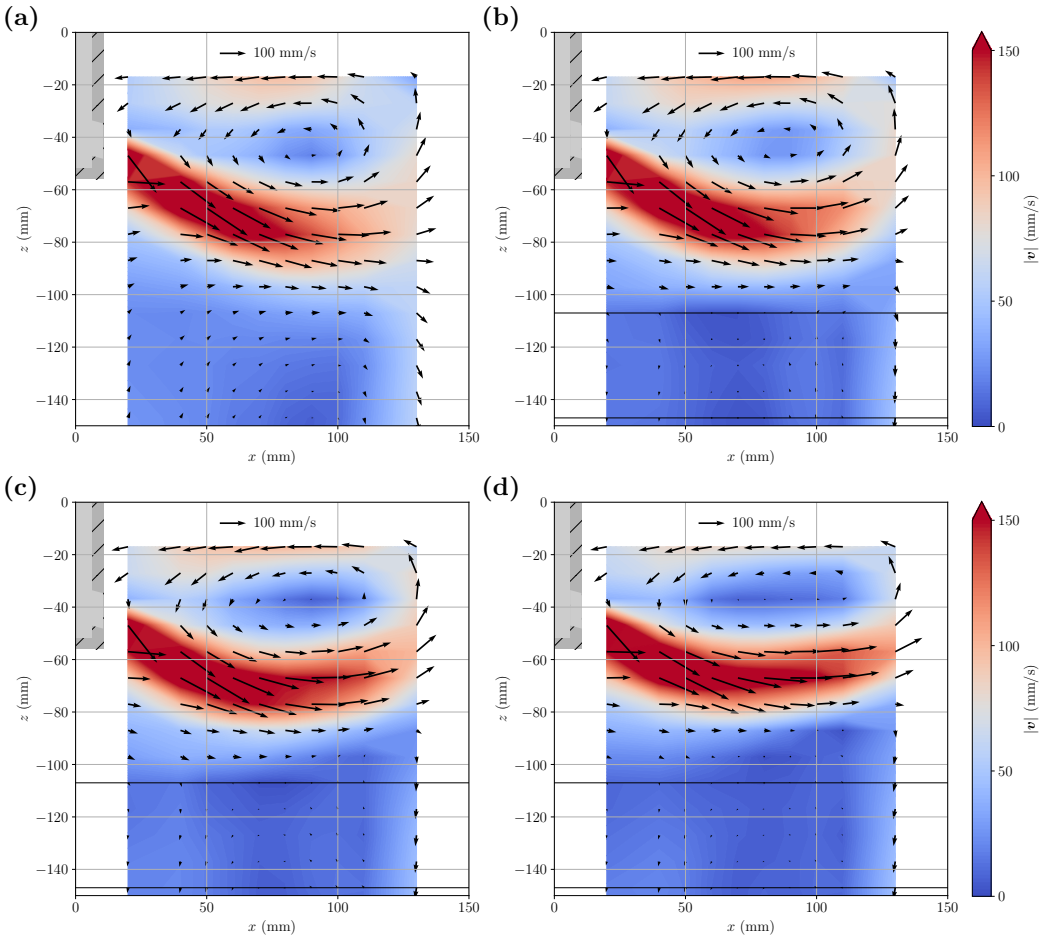

Fig. 8 Vector and contour plot of the time-averaged velocity distribution in the top part of the mold, measured for different magnetic flux densities B (a) EMBr off, (b) 102 mT, (c) 190 mT, (d) 318 mT of the EMBr. The brake is positioned at $z_{brake} = -127$ mm, the edges of the activated EMBr pole shoe are marked by horizontal black lines.

In turn, the intensity of the upper roll increases, which leads to the observed increased horizontal velocities below the free surface.

3.3 Influence of the SEN Immersion Depth

The immersion depth of the submerged entry nozzle h_{im} is an important parameter which is often varied during the casting process.

Variations of the meniscus level were carried out in our mold model to reproduce two different cases (Figure 9):

- Series A: The first series (Figure 9(a)) represents the variation of the meniscus level in the mold. Here, the EMBr position with respect to the SEN is kept constant, that means the distance from the electromagnetic brake to the meniscus level, z_{brake}, changes in the same way as the SEN immersion depth h_{im}.
- Series B: The distance between EMBr and meniscus, z_{brake}, is a constant in the second series (Figure 9(b))

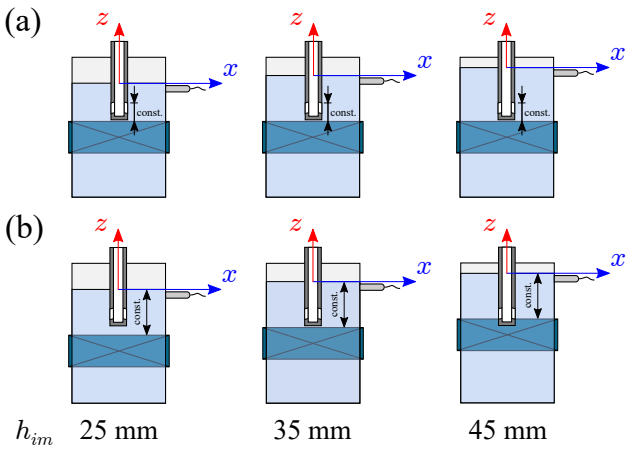

Fig. 9 Schematic illustration of two cases to set a different immersion depth: (a) The level in the mold is varied. (b) Level and brake position are changed, representing a relative vertical movement of tundish and SEN compared to the mold.

which considers a vertical relocation of tundish and SEN relative to the mold and thus to the EMBr.

For both cases the level in the tundish has been adjusted to maintain a constant drop height of the fluid from the tundish to the free surface in the mold. The reference case is defined as a brake position of $z_{brake} = -77\,\text{mm}$ and an immersion depth of $h_{im} = 35\,\text{mm}$.

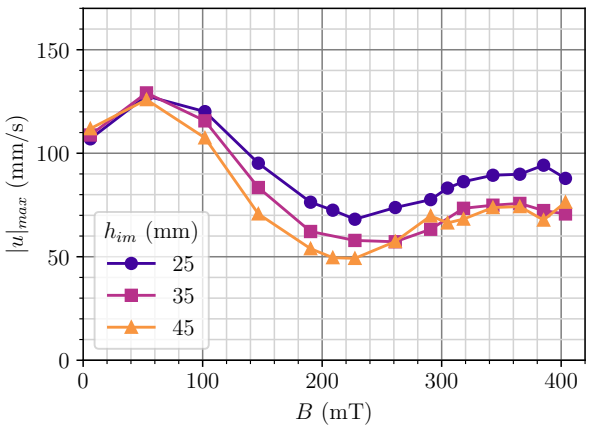

Fig. 10 Maximum of the time-averaged horizontal velocity $|u|_{max}$, measured at $z = -7\,\text{mm}$ for different immersion depths h_{im} and magnetic flux densities B. Here, the immersion depth was changed by changing the level in the mold (series A).

Figure 10 shows the maximum of the time-averaged horizontal velocity $|u|_{max}$, measured along the top measuring line at $z = -7\,\text{mm}$ as a function of the magnetic flux density B for three different immersion depths h_{im}. These measurements are assigned to the series A, where the immersion depth h_{im} is varied by changing the level in the mold. The distance between the top of the SEN port and the center of the EMBr, $|z_{brake}| - h_{im} = 42\,\text{mm}$, is kept constant. With respect to the velocity value for the deactivated brake ($110\,\text{mm/s}$), all three curves reveal the highest reductions of the near-meniscus velocities for moderate magnetic flux densities around $220\,\text{mT}$. The value $|u|_{max}$ declines slightly with increasing immersion depth, which is intuitive since the path length from the SEN port to the free surface is increased. This should increase the effect of electromagnetic and viscous dissipation in terms of velocity reduction.

Figure 11 shows the time-averaged velocity field in the upper part of the mold for the highest and lowest values of the immersion depth h_{im} and different magnetic flux densities B for series A. In the case of the reduced immersion depth, there is less space for the upper roll between the jet and the free surface. However, further changes in the flow pattern due to the variation of the immersion depth h_{im} are only marginal. The effect of the magnetic field does not differ fundamentally from that described in the previous chapter.

In a next step, the corresponding results for series B will be considered. Figure 12 illustrates the evolution of the maximum of the time-averaged near-surface velocity $|u|_{max}$ for a varying magnetic flux density B at three different immersion depths h_{im}. The shape of the three curves is similar to that of the measurements for series A. For magnetic field intensities of $B \geq 100\,\text{mT}$, $|u|_{max}$ increases with decreasing immersion depth h_{im}. For $B > 200\,\text{mT}$ the velocities for all immersion depths are lower than for the case with deactivated EMBr.

Figure 13 shows the time-averaged plots of the velocity distribution in the upper part of the mold for series B. The comparison between the situations for $h_{im} = 25\,\text{mm}$ and $45\,\text{mm}$ reveals a qualitatively different appearance of the jet if a magnetic field is applied. This becomes especially clear for the highest magnetic flux density of $B = 404\,\text{mT}$. The reason is the variation of the distance between electromagnetic brake and SEN port. The shape of the jet is much more affected when the EMBr is positioned directly at the bottom of the SEN ports. In addition, the resulting shape of the jet is completely different at different magnetic field strengths. It is noteworthy that in the case of the high magnetic field at $B = 404\,\text{mT}$, the jet is initially forced out of the magnetic field area significantly upwards, but after a certain path length it aligns horizontally again. The jet gets an S-shape. In contrast, the jet seems to be dragged into the magnetic field area at smaller field strengths as it has already been observed in Figure 7.

3.4 Velocity and Shape of the Submerged Jet

In this section, we are particularly interested in the characteristics of the submerged jet with respect to its velocity and shape. Both properties are key indicators in assessing the actual braking effect of the EMBr on the jet flow. Here, we reconsider the measurements made for the reference case where the immersion depth is $h_{im} = 35\,\text{mm}$ and the brake is positioned at $z_{brake} = -77\,\text{mm}$.

Due to the minimal distance of $10\,\text{mm}$ between adjacent UDV transducers, it is not possible to precisely measure the location and velocity of the jet, $z_{jet}(x)$ and $v_{jet}(x)$ respectively. In the worst case, the the jet is located between two measurement lines.

To overcome this limitation, we extend the falling and rising edge of the two-dimensional velocity magnitude $|\mathbf{v}(x,z)|$ in z-direction. The intersection of these lines, defines $z_{jet}(x)$ and $v_{jet}(x)$. Figure 14 shows the time-averaged velocity magnitude at three different x-locations along z for an exemplary measurement. As seen, with the linear interpolation it is possible to estimate the location of the jet z_{jet} more precisely

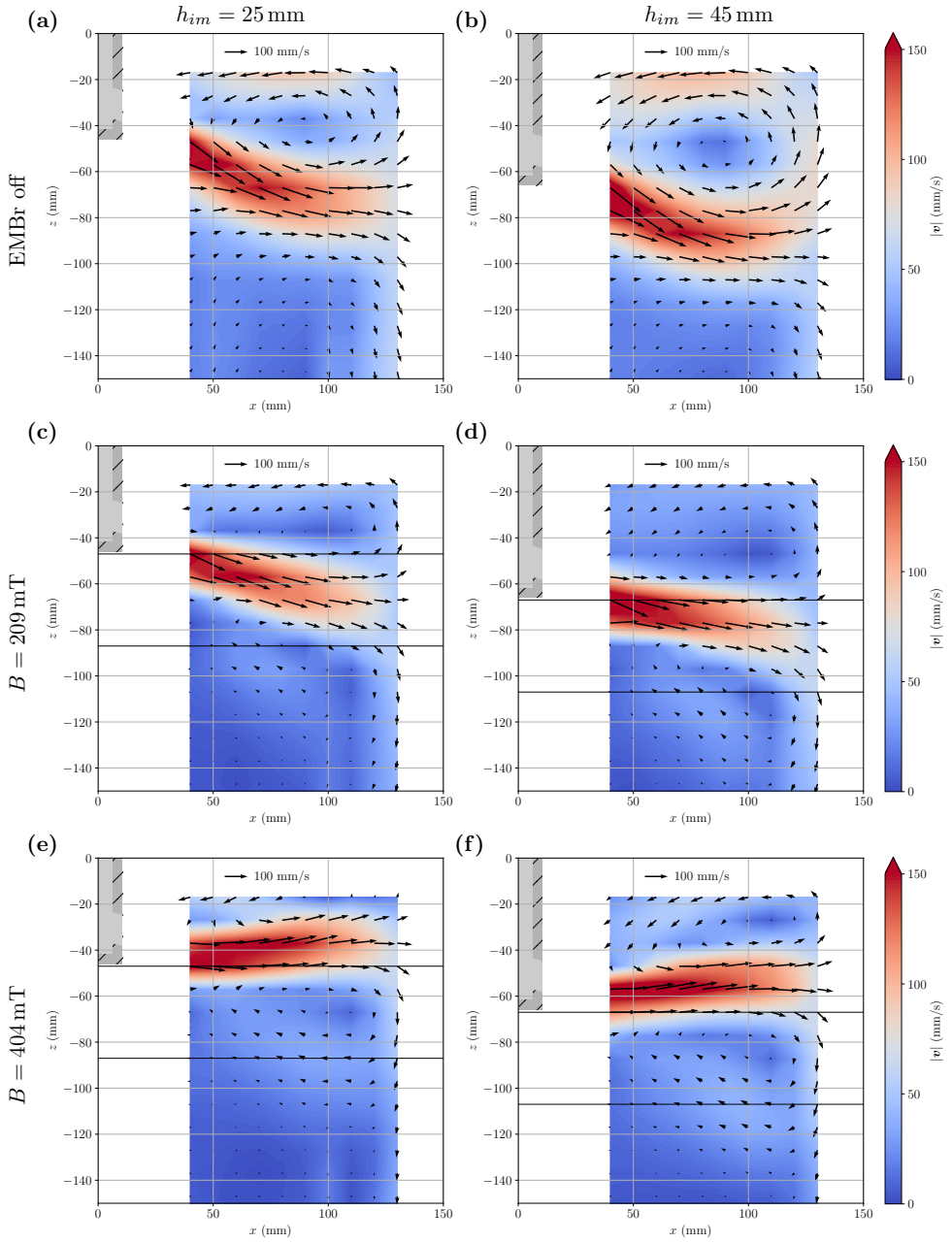

Fig. 11 Vector and contour plot of the time-averaged velocity distribution in the top part of the mold for different immersion depths h_{im} and magnetic flux densities B representing the case where the level in the mold is changed (series A, c.f. Figure 9(a)). The immersion depth is increased from left to right: (a,c,e) 25 mm and (b, d, f) 45 mm. The magnetic flux density is increased from top to bottom: (a,b) EMBr off, (c,d) 209 mT and (e,f) 404 mT. The edges of the activated EMBr pole shoe are marked by horizontal black lines.

between two measurement lines. The corresponding velocity value v_{jet} is likely to be overestimated due to the application of a linear interpolation. Although, it improves the results when the jet is located between two measurement lines.

Since only the velocity magnitude is interpolated, the velocity angle of the jet $\alpha_{jet}(x) = \arctan(w/u)$ is not available from the interpolation, but taken from the point where the highest velocity magnitude is measured. Therefore, α_{jet} is mostly taken from a point slightly above or below the actual jet position z_{jet}.

Figure 15 shows exemplary velocity vector fields associated with the case of the deactivated EMBr and two experiments where a moderate ($B = 190\,\mathrm{mT}$) and a strong magnetic field ($B = 404\,\mathrm{mT}$) are applied. The interpolated location of the jet z_{jet} is indicated by a line plot, while the location where the highest velocities were actually measured, are

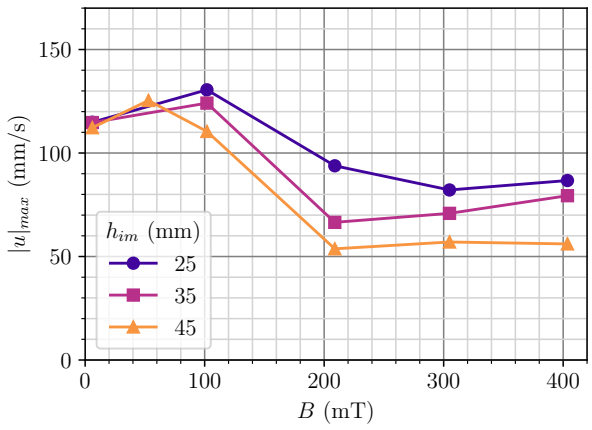

Fig. 12 Maximum of the time-averaged horizontal velocity $|u|_{max}$, measured at $z = -7$ mm for different immersion depths h_{im} and magnetic flux densities B. Here, SEN and tundish positions are changed with respect to the mold and the EMBr (series B).

represented by gray dots. The necessity to interpolate the location of the jet becomes obvious when comparing these two representations. Finally, the colors of the contour plot indicate the vorticity ω, which is calculated as the rotation of the two-dimensional velocity field ($v = 0$):

$$\omega = \nabla \times \mathbf{v} = (\partial_z u - \partial_x w)\mathbf{e_y} \tag{7}$$

In all plots a white band of vanishing vorticity $\omega \approx \mathbf{0}$ can be identified between the regions of intense vorticity. This area is associated with the course of the jet after leaving the SEN port.

Without applied magnetic field (Figure 15(a)) one vortex rotating in counter-clockwise direction occurs above the jet while the lower region is dominated by negative vorticity corresponding to a clockwise rotation of the flow. This structure is basically retained in the case of the EMBr, but the areas of high vorticity converge closer to the jet. For a magnetic flux density of 190 mT (Figure 15(b)), the jet divides the mold almost under an angle defined by the inclination angle of the SEN port. A sufficiently strong magnetic field causes the formation of a further weakly counter-rotating vortex in the lower central part of the mold (Figures 15(b) and (c)). This region of low positive rotation moves with increasing magnetic flux density toward the narrow face of the mold (Figure 15(c)) and the region of positive rotation above the jet is intensified but reduced in z-direction.

To obtain more quantitative information regarding the shape and the velocity of the jet under the influence of different magnetic flux densities we will now take a closer look at some data extracted from the jet region.

The estimated location of the jet $z_{jet}(x)$ is depicted in Figure 16 as a function of the magnetic flux density B of the EMBr. In principle, three different shapes of the jet can be distinguished:

- Low magnetic field strength ($B < 150$ mT): The jet direction initially points downwards. As the distance from the nozzle increases, the angle becomes flatter, and finally the direction is reversed, i.e. just before hitting the side wall, the jet is directed upwards. This form can also be referred to a "banana"-shape.
- Medium magnetic field strength ($B \approx 200$ mT): A jet with a rather straight shape appears. Its angle matches approximately that of the SEN port.
- High magnetic field strength ($B > 300$ mT): The jet leaves the port in a nearly horizontal direction and then bends slightly downwards. In cases where the EMBr is positioned close to the ports, the jet is bent so high first and then down again that its shape is reminiscent of a horizontal "S"-shape.

The corresponding estimated center velocities of the jet v_{jet} are shown in Figure 17. In cases of a deactivated EMBr or at weak magnetic fields, the velocity decreases gradually with growing distance from the nozzle port which is associated with the progressing dissipation of the jet. It is interesting to note, that the application of strong magnetic fields lead to an increase of the jet velocity in a region close to the SEN ($x < 90$ mm). At larger distances from the nozzle the jet velocities decrease again, but still remain slightly above the values for smaller magnetic fields.

Finally, Figure 18 shows α_{jet}, the angle of the two-dimensional velocity vector $\mathbf{v}$ determined in the jet region, for different magnetic fields B along the horizontal coordinate x. In accordance with the previous observations, the different shapes of the jet can also be identified from α_{jet}. The "banana"-shape occurring at low magnetic flux densities is identified by the linear growth of α_{jet} from negative values of around -30 deg at $x = 40$ mm to a positive velocity angle of 15 deg at $x = 120$ mm. The jet is initially directed down and then deflected upwards. The straight shape of the jet for medium values of B is characterized by an almost constant jet angle of $\alpha_{jet} \approx -15$ deg which coincides with the port angle of the SEN. In the case of high magnetic fields, the "S"-shape results from the jet leaving the ports downwards, then running almost straight or slightly upward for a short distance before being directed down again. This is reflected by a change of α_{jet} from negative to slightly positive and back to negative values with increasing distance from the SEN.

4 Discussion

The data collected by the systematic measurements in this study enables us to take a closer look at the braking effect

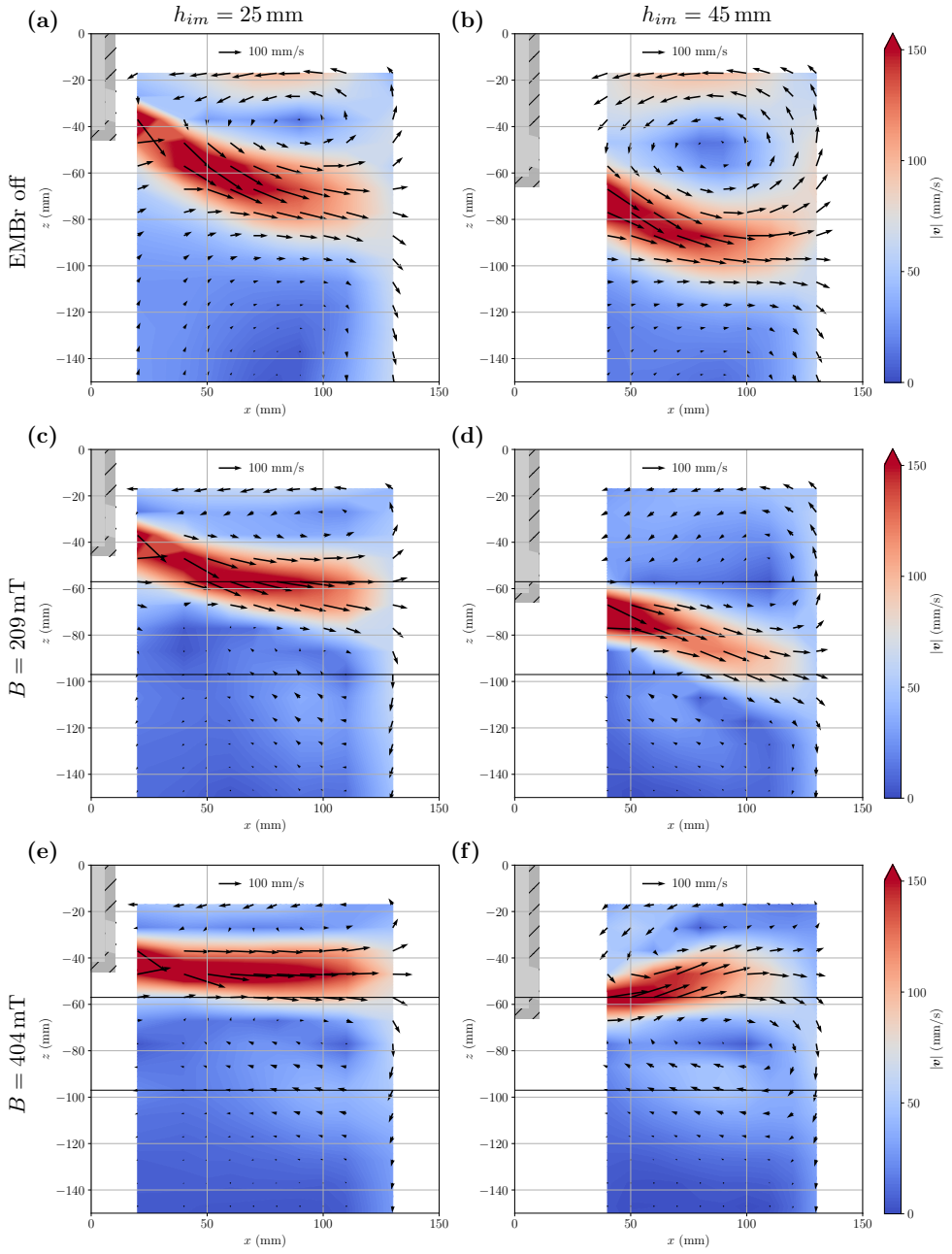

Fig. 13 Vector and contour plot of the time-averaged velocity distribution in the top part of the mold for different immersion depths h_{im} and magnetic flux densities B representing the case where tundish and SEN positions are shifted relative to the mold and EMBr (series B, c.f. Figure 9(b)). The immersion depth is increased from left to right: (a,c,e) 25 mm and (b, d, f) 45 mm. The magnetic flux density is increased from top to bottom: (a,b) EMBr off, (c,d) 209 mT and (e,f) 404 mT. The edges of the activated EMBr pole shoe are marked by horizontal black lines.

of the magnetic field on the flow in the mold. In particular, the focus is on the surface region, since an uncontrolled flow in this area is considered as a main reason for many casting defects. Figure 5 shows how the maximum values of the horizontal flow component just below the free surface change depending on the EMBr position. It can be observed that the near-surface velocity is reduced for all magnetic flux densities if the magnet is installed so that the pole pieces cover the free surface line ($z_{brake} > -10\,\mathrm{mm}$). Obviously, the magnetic field in an upper position provides a slowdown of the flow at the surface. Flow field measurements for the upper magnetic field positions reveal a magnetic field impact on the entire upper roll of the flow structure (not shown here). The jet gets a straight shape and its vertical extension is reduced. This evidently results in the lower roll being fed more strongly by the jet and thus having a higher flow

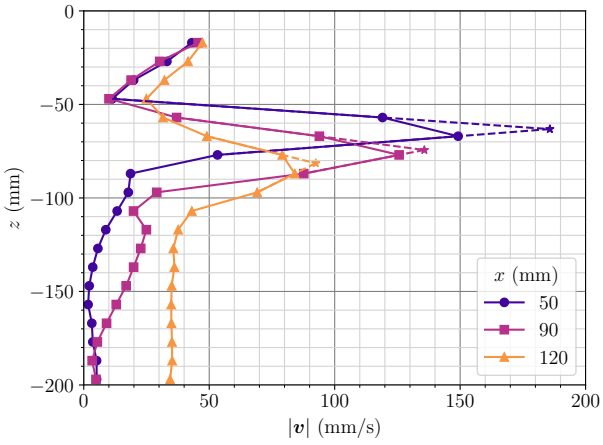

Fig. 14 Time-averaged two-dimensional velocities at three x-locations along z for $B = 190\,\mathrm{mT}$ and a brake position of $z_{brake} = -77\,\mathrm{mm}$. The result of the linear interpolation is indicated by a star symbol and represents the jet's location and velocity z_{jet} and v_{jet} respectively.

intensity. This constellation is obviously advantageous for achieving low near-surface flow velocities. However, it must be checked to what extent sufficient heat transport from the jet region towards the meniscus is still ensured in order to prevent freezing on the narrow side wall.

The result of a gradual lowering of the brake position shows that a deceleration of the velocities beneath the surface can not be achieved if the magnetic field is not strong enough. The velocity values for $B = 109\,\mathrm{mT}$ are even significantly higher than those in the reference case without magnetic field. Figure 5 indicates a reduction of the maximum values of the near-surface velocity by means of a sufficiently strong magnetic field, if the center position of the EMBr is fixed in a range of $-40\,\mathrm{mm} \geq z_{brake} \geq -100\,\mathrm{mm}$. In case of even lower positioning of the EMBr, this reduction effect is lost again. The cause of the latter is to be found in the fact that a magnetic field which is positioned clearly below the SEN obviously dampens the flow in the lower region of the mold (see Figure 8). This is accompanied by a significant reinforcement of the upper vortex in the double-roll structure, which then inevitably means an increase in the near-surface velocity.

In a part of the parameter range for which a significant reduction of the time-averaged speed maxima is achieved, there is an overlap of the SEN ports with the pole shoe of the EMBr ($-20\,\mathrm{mm} \geq z_{brake} \geq -60\,\mathrm{mm}$). For such a constellation the occurrence of strong velocity fluctuations was observed[36]. The strong velocity perturbations are associated with distinct fluctuations of the jet angle, whereas the jet oscillations on both sides of the SEN are almost opposite in phase[23]. However, such an unstable flow is not considered to be very beneficial to the casting process. Ultimately, the positioning of the EMBr just below the SEN ports appears to be the optimal solution for achieving a significant reduction of the horizontal melt flow at the free surface.

These results confirm the observations reported by Moon et al.[25] and Thomas et al.[35]. Our data are also compatible with the numerical results obtained by Li & Tsukihashi[20], which show a reduction in the near-surface velocity with increasing magnetic field strength for an EMBr position below the SEN in thin-slab casting. However, there is an obvious contradiction to the results of[7] and[6], whose numerical simulations indicate an increase in the near-surface velocity with decreasing EMBr position.

The question still needs to be answered, how the changes in the magnetic field positions affect the flow structures in detail. Our flow measurements reveal distinct deformations of the jet, whereby the resulting structures can clearly differ. A strong correlation between the velocity below the meniscus $|u|_{max}$ and the angle difference of the jet $\Delta\alpha_{jet} = \alpha_{jet}(x = 110\,\mathrm{mm}) - \alpha_{jet}(x = 50\,\mathrm{mm})$, which is a measure for the shape of the jet, can be observed in Figure 19. In contrast, the velocity of the jet v_{jet} decreases only slightly before it increases for $B > 261\,\mathrm{mT}$, while the velocity below the meniscus decreases first substantially and then rises only slightly with increasing B. So obviously, there is no immediate connection between the jet velocity and the near-surface flow. The difference of the angle of the jet $\Delta\alpha_{jet}$ shows a very similar behavior to that of $|u|_{max}$. From this it can be concluded that mainly the modification of the jet shape is responsible for the reduction of the surface velocity. Only for the large magnetic fields ($B > 261\,\mathrm{mT}$) there seems to be a direct link between $|u|_{max}$ and v_{jet}. This is suggested by the similarity with respect to the course of both curves. The almost horizontal alignment of the jet (c.f. Figure 18) and the increasing jet velocity might be the reason for this slight enhancement in surface velocity at high magnetic fields. There is no consistent reflection of this effect by numerical studies in the literature. While Miao et al.[23] or Chaudhary et al.[1] show also a significant curvature of the jet under the influence of the magnetic field, this phenomenon is not visible in many other numerical data.

Figure 19 and all results in their entirety reveal an amazing aspect: Obviously, a direct effect of the magnetic field in terms of a significant braking of the velocity field, in particular of the submerged jet, is hardly detectable. There are parameter ranges in which even a significant increase of the jet velocity with increasing magnetic field can be observed. The variation of the jet velocity with the horizontal distance from the SEN port can be seen in Figure 17. Usually, it is to be expected that the jet will be decelerated continuously with increasing path length. This is exactly what is observed in measurements with deactivated EMBr and at low field strengths. However, the application of strong magnetic fields causes the jet to accelerate before it really slows down. This finding can only be explained by a restriction of the jet cross-

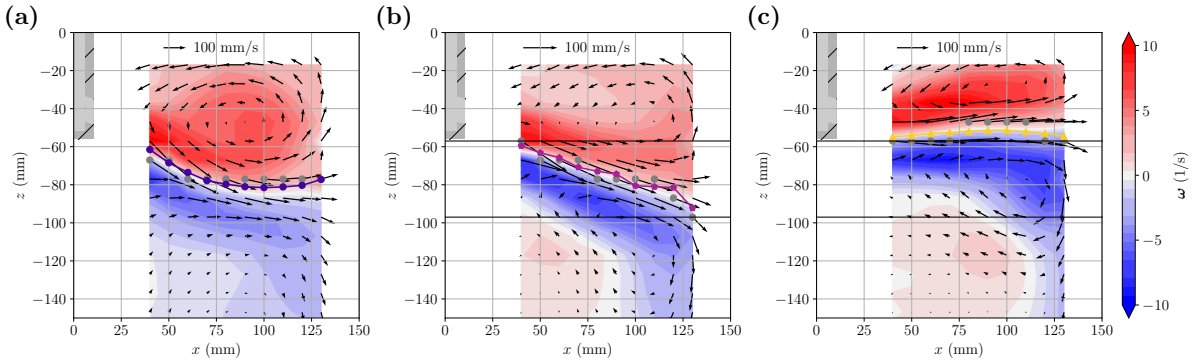

Fig. 15 Time-average vector plot of the two-dimensional velocity distribution in the mold. The colors of the contour plot depict the vorticity ω. The gray dots indicate the location where the maximum velocity along x was measured, while the line plot indicates the interpolated position of the jet z_{jet}. The magnetic flux density B of the EMBr is (a) EMBr off, (b) 190 mT and (c) 404 mT. The edges of the activated EMBr pole shoe are marked by horizontal black lines.

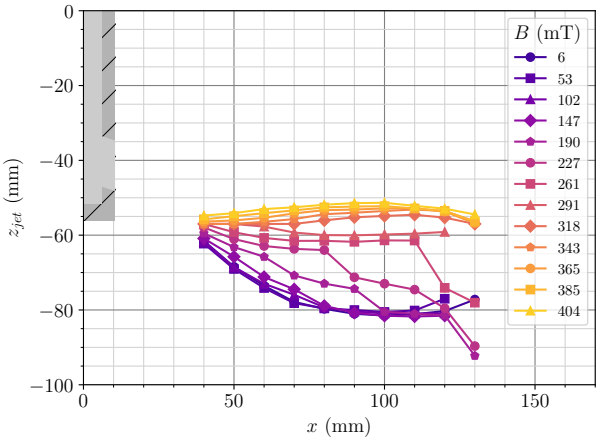

Fig. 16 Interpolated vertical location of the jet z_{jet} at different position x in the mold for varying magnetic flux density B at $z_{brake} = -77$ mm and $h_{im} = 35$ mm.

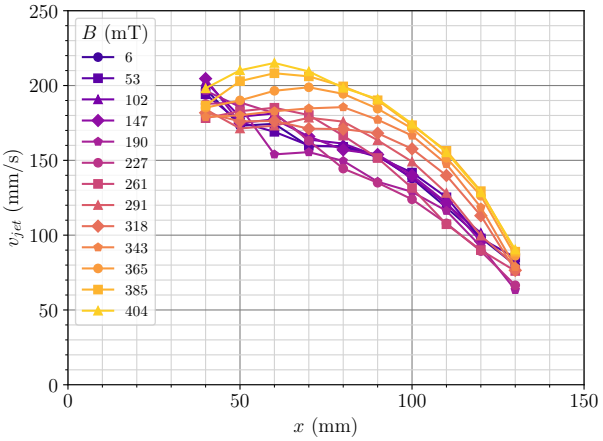

Fig. 17 Interpolated velocity of the jet v_{jet} at different position x in the mold for varying magnetic flux density B at $z_{brake} = -77$ mm and $h_{im} = 35$ mm.

section. In fact, such a focusing of the jet becomes apparent in several plots of the flow structure.

Thus, in summary, the essential mechanism of an EMBr for flow control in a continuous casting mold is not that the flow is immediately decelerated, but that a restructuring of the flow field takes place. In this context, it is clear that the shape of the magnetic field and its position has a decisive influence on the behavior of the mold flow. Further parameters are the magnetic flux density, the SEN geometry or the immersion depth. The flow structure is primarily modified by changing the shape and the cross-section of the jet. This is extremely complex in detail, for instance, the installation of the EMBr at the meniscus has not only an effect on the submeniscus velocities, but also on the shape of the jet. Likewise, an EMBr at low positions far beyond the nozzle ports can influence the jet and in turn the near-surface flow. Another issue is the decay of the magnetic field strength beyond the pole faces because the EMBr also produces a considerable magnetic field outside the pole piece area. In this area an inhomogeneous field distribution has to be assumed. The behavior of submerged jets in an inhomogeneous magnetic field needs further investigation.

5 Conclusions

An experimental investigation of the velocity distribution in a slab mold for continuous casting of steel under the influence of an Electromagnetic Brake (EMBr) has been performed in a physical liquid metal model, the Mini-LIMMCAST facility of HZDR. The setup with a mold cross-section of $300 \times 35\,\mathrm{mm}^2$ and a realistic geometry of the Submerged Entry Nozzle (SEN) represents downscaled industrial continuous

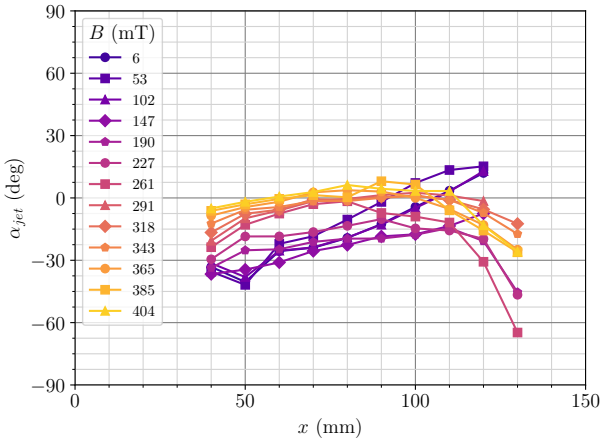

Fig. 18 Angle α_{jet} of the two-dimensional velocity vector **v** close to the jet at different position x in the mold for varying magnetic flux density B at $z_{brake} = -77\,\text{mm}$ and $h_{im} = 35\,\text{mm}$.

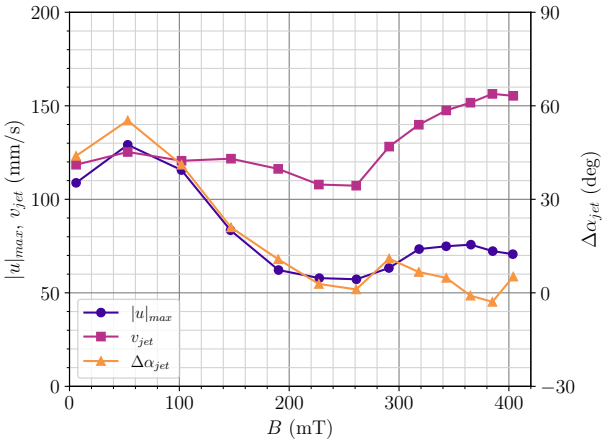

Fig. 19 Velocity below the meniscus $|u|_{max}$ and jet velocity $v_{jet}(x = 110\,\text{mm})$ as well as the difference of the angle of the jet $\Delta\alpha_{jet} = \alpha_{jet}(x = 110\,\text{mm}) - \alpha_{jet}(x = 50\,\text{mm})$ over the magnetic flux density B of the EMBr at $z_{brake} = -77\,\text{mm}$ and $h_{im} = 35\,\text{mm}$.

casters. The EMBr generates magnetic flux densities up to 404 mT with a uniform field distribution over the whole mold width. The vertical position of the EMBr can be easily varied in small steps along the mold. The two-dimensional velocity distribution in the center plane of the mold has been measured by means of the Ultrasound Doppler Velocimetry (UDV). This study examines a wide range in the parameter space, spanned by highly resolved variations of the vertical EMBr position and the strength of the magnetic field.

Our experimental results allow to conclude the following:

1. The horizontal velocities measured directly below the free surface are highly dependent on the position of the EMBr. These velocities can effectively be reduced by more than 50 % if the EMBr is installed at an optimal position. On the other hand, other positions of the electromagnetic brake may also increase the near-surface velocities compared to the case with deactivated brake.
2. The decisive mechanism for modifying the flow velocity at the surface is a restructuring of the global flow field, in particular a variation of the shape and the cross-section of the jet, rather than directly decelerating the flow due to the magnetic field.
3. With increasing strength of the EMBr the jet is moved upward and flows almost horizontally from the SEN port to the narrow-face of the mold.
4. Three distinct shapes of the jet have been observed under the influence of different strengths of the EMBr: I) a "banana"-shape for no or low magnetic flux densities, II) a straight shape for medium strengths of the EMBr and III) a horizontal S-shape, when a very high magnetic flux density expels the jet from the EMBr zone.
5. Given the mechanism of flow control, it is obvious that the positioning of the magnetic field plays a very sensitive role. The homogeneity of the magnetic field and its distribution beyond the pole shoes are also very important in this context and have to be taken into account for optimizing the EMBr parameters in the industrial process.

Further investigations should focus on the effect of the EMBr position on the temporal features of the flow field and the impact of the electrical conductivity of the side walls.

References

1. Chaudhary, R., Thomas, B.G., Vanka, S.P.: Effect of Electromagnetic Ruler Braking (EMBr) on Transient Turbulent Flow in Continuous Slab Casting using Large Eddy Simulations. Metall. Mater. Trans. B **43**(3), 532–553 (2012). DOI 10.1007/s11663-012-9634-6
2. Cho, S.M., Kim, S.H., Thomas, B.G.: Transient Fluid Flow during Steady Continuous Casting of Steel Slabs: Part I. Measurements and Modeling of Two-phase Flow. ISIJ Int. **54**(4), 845–854 (2014). DOI 10.2355/isijinternational.54.845
3. Cho, S.M., Thomas, B.G.: Electromagnetic Forces in Continuous Casting of Steel Slabs. Metals **9**(4), 471 (2019). DOI 10.3390/met9040471
4. Eckert, S., Cramer, A., Gerbeth, G.: Velocity Measurement Techniques for Liquid Metal Flows. In: R. Moreau (ed.) Magnetohydrodynamics, vol. 80, pp. 275–294. Springer Netherlands, Dordrecht (2007). DOI 10.1007/978-1-4020-4833-3_17
5. Evonik Industries AG: Technical Information PLEXIGLAS® (2013)
6. Garcia-Hernandez, S., Morales, R.D., Torres-Alonso, E.: Effects of EMBr position, mould curvature and

slide gate on fluid flow of steel in slab mould. Ironmaking Steelmaking **37**(5), 360–368 (2010). DOI 10.1179/030192309X12595763236969
7. Haiqi, Y., Baofeng, W., Huiqin, L., Jianchao, L.: Influence of electromagnetic brake on flow field of liquid steel in the slab continuous casting mold. Journal of Materials Processing Technology **202**(1-3), 179–187 (2008). DOI 10.1016/j.jmatprotec.2007.08.054
8. Han, S.W., Cho, H.J., Jin, S.Y., Sedén, M., Lee, I.B., Sohn, I.: Effects of Simultaneous Static and Traveling Magnetic Fields on the Molten Steel Flow in a Continuous Casting Mold. Metall. Mater. Trans. B **49**(5), 2757–2769 (2018). DOI 10.1007/s11663-018-1356-y
9. Harada, H., Toh, T., Ishii, T., Kaneko, K., Takeuchi, E.: Effect of Magnetic Field Conditions on the Electromagnetic Braking Efficiency. ISIJ Int. **41**(10), 1236–1244 (2001)
10. Hibbeler, L.C., Thomas, B.G.: Mold Slag Entrainment Mechanisms in Continuous Casting Molds. Iron Steel Technol. **10**, 121–136 (2013)
11. Ho, C.Y., Chu, T.K.: Electrical resistivity and thermal conductivity of nine selected AISI stainless steels. Tech. Rep. 45, Cindas, Purdue University, West Lafayette (1977)
12. Hwang, Y.S., Cha, P.R., Nam, H.S., Moon, K.H., Yoon, J.K.: Numerical Analysis of the Influences of Operational Parameters on the Fluid Flow and Meniscus Shape in Slab Caster with EMBR. ISIJ Int. **37**(7), 659–667 (1997). DOI 10.2355/isijinternational.37.659
13. Idogawa, A., Sugizawa, M., Takeuchi, S., Sorimachi, K., Fujii, T.: Control of molten steel flow in continuous casting mold by two static magnetic fields imposed on whole width. Materials Science and Engineering: A **173**(1-2), 293–297 (1993). DOI 10.1016/0921-5093(93)90231-3
14. Jeon, Y.J., Sung, H.J., Lee, S.: Flow Oscillations and Meniscus Fluctuations in a Funnel-Type Water Mold Model. Metall. Mater. Trans. B **41**(1), 121–130 (2010). DOI 10.1007/s11663-009-9318-z
15. Ji, C., Li, J., Tang, H., Yang, S.: Effect of EMBr on Flow in Slab Continuous Casting Mold and Evaluation Using Nail Dipping Measurement. Steel Res. Int. **84**(3), 259–268 (2013). DOI 10.1002/srin.201200117
16. Jimbo, I., Cramb, A.W.: The density of liquid iron-carbon alloys. Metall. Trans. B **24**(1), 5–10 (1993). DOI 10.1007/BF02657866
17. Korolczuk-Hejnak, M., Migas, P., Ślęzak, W.: Determination of the liquid steel viscosity curves using a high temperature rheometer. J. Phys.: Conf. Ser. **602**, 012,037 (2015). DOI 10.1088/1742-6596/602/1/012037
18. Krautkrämer, J., Krautkrämer, H.: Werkstoffprüfung mit Ultraschall, 5 edn. Springer, Berlin, Heidelberg (1986). DOI 10.1007/978-3-662-10909-0
19. Kubota, J., Kubo, N., Ishii, T., Suzuki, M., Aramaki, N., Nishimachi, R.: Steel Flow Control in Continuous Slab Caster Mold by Traveling Magnetic Field. NKK Technical Review **85**, 9 (2001)
20. Li, B., Tsukihashi, F.: Effects of Electromagnetic Brake on Vortex Flows in Thin Slab Continuous Casting Mold. ISIJ Int. **46**(12), 1833–1838 (2006). DOI 10.2355/isijinternational.46.1833
21. Li, Z., Mukai, K., Zeze, M., Mills, K.C.: Determination of the surface tension of liquid stainless steel. J. Mater. Sci. **40**(9-10), 2191–2195 (2005). DOI 10.1007/s10853-005-1931-x
22. Liu, Z., Vakhrushev, A., Wu, M., Karimi-Sibaki, E., Kharicha, A., Ludwig, A., Li, B.: Effect of an Electrically-Conducting Wall on Transient Magnetohydrodynamic Flow in a Continuous-Casting Mold with an Electromagnetic Brake. Metals **8**(8), 609 (2018). DOI 10.3390/met8080609
23. Miao, X., Timmel, K., Lucas, D., Ren, Z., Eckert, S., Gerbeth, G.: Effect of an Electromagnetic Brake on the Turbulent Melt Flow in a Continuous-Casting Mold. Metall. Mater. Trans. B **43**(4), 954–972 (2012). DOI 10.1007/s11663-012-9672-0
24. Miki, Y., Takeuchi, S.: Internal Defects of Continuous Casting Slabs Caused by Asymmetric Unbalanced Steel Flow in Mold. ISIJ Int. **43**(10), 1548–1555 (2003). DOI 10.2355/isijinternational.43.1548
25. Moon, K.H., Shin, H.K., Kim, B.J., Chung, J.Y., Hwang, Y.S., Yoon, J.K.: Flow Control of Molten Steel by Electromagnetic Brake in the Continuous Casting Mold. ISIJ Int. **36**(Suppl), S201–S203 (1996). DOI 10.2355/isijinternational.36.Suppl_S201
26. Morley, N.B., Burris, J., Cadwallader, L.C., Nornberg, M.D.: GaInSn usage in the research laboratory. Rev. Sci. Instrum. **79**(5), 056,107 (2008). DOI 10.1063/1.2930813
27. Odenthal, H.J., Pfeifer, H., Lemanowicz, I., Gorissen, R.: Simulation of the submerged energy nozzle-mold water model system using laser-optical and computational fluid dynamics methods. Metall. Mater. Trans. B **33**(2), 163–172 (2002). DOI 10.1007/s11663-002-0002-9
28. Okazawa, K., Sawada, I., Harada, H., Toh, T., Takeuchi, E.: Characteristics of Molten Steel Jet Flow in a Continuous Casting Mold with Electromagnetic Brake Technique. Tetsu-to-Hagane **84**(7), 490–495 (1998). DOI 10.2355/tetsutohagane1955.84.7_490
29. Plevachuk, Y., Sklyarchuk, V., Eckert, S., Gerbeth, G., Novakovic, R.: Thermophysical Properties of the Liquid Ga–In–Sn Eutectic Alloy. J. Chem. Eng. Data **59**(3), 757–763 (2014). DOI 10.1021/je400882q
30. Signal Processing S. A.: DOP3000-3010 Series User's Manual. Switzerland (2017)
31. Singh, R., Thomas, B.G., Vanka, S.P.: Effects of a Magnetic Field on Turbulent Flow in the Mold Region of a

Steel Caster. Metall. Mater. Trans. B **44**(5), 1201–1221 (2013). DOI 10.1007/s11663-013-9877-x
32. Szekely, J., Yadoya, R.T.: The physical and mathematical modeling of the flow field in the mold region in continuous casting systems: Part I. model studies with aqueous systems. Metall. Trans. **3**(10), 2673–2680 (1972). DOI 10.1007/BF02644243
33. Takeda, Y.: Development of an ultrasound velocity profile monitor. Nuclear Engineering and Design **126**(2), 277–284 (1991). DOI 10.1016/0029-5493(91)90117-Z
34. Thomas, B.G.: Review on Modeling and Simulation of Continuous Casting. Steel Res. Int. **89**(1), 1700,312 (2018). DOI 10.1002/srin.201700312
35. Thomas, B.G., Singh, R., Vanka, S.P., Timmel, K., Eckert, S., Gerbeth, G.: Effect of Single-Ruler Electromagnetic Braking (EMBr) Location on Transient Flow in Continuous Casting. J. Manuf. Sci. Prod. **15**(1) (2015). DOI 10.1515/jmsp-2014-0047
36. Timmel, K., Eckert, S., Gerbeth, G.: Experimental Investigation of the Flow in a Continuous-Casting Mold under the Influence of a Transverse, Direct Current Magnetic Field. Metall. Mater. Trans. B **42**(1), 68–80 (2011). DOI 10.1007/s11663-010-9458-1
37. Timmel, K., Eckert, S., Gerbeth, G., Stefani, F., Wondrak, T.: Experimental Modeling of the Continuous Casting Process of Steel Using Low Melting Point Metal Alloys - the LIMMCAST Program. ISIJ Int. **50**(8), 1134–1141 (2010). DOI 10.2355/isijinternational.50.1134
38. Timmel, K., Kratzsch, C., Asad, A., Schurmann, D., Schwarze, R., Eckert, S.: Experimental and Numerical Modeling of Fluid Flow Processes in Continuous Casting: Results from the LIMMCAST-Project. IOP Conf. Ser.: Mater. Sci. Eng. **228**, 012,019 (2017). DOI 10.1088/1757-899X/228/1/012019
39. VDI (ed.): VDI-Wärmeatlas, 11 edn. Springer Vieweg, Berlin, Heidelberg (2013). DOI 10.1007/978-3-642-19981-3
40. Yu, Z., Zhang, Z.Q., Ren, Z.M.: Effect of flow control mold on flow field during high-speed continuous casting. Adv. Manuf. **5**(3), 271–278 (2017). DOI 10.1007/s40436-017-0183-8
41. Zhang, T., Yang, J., Jiang, P.: Measurement of Molten Steel Velocity near the Surface and Modeling for Transient Fluid Flow in the Continuous Casting Mold. Metals **9**(1), 36 (2019). DOI 10.3390/met9010036
42. Zhang, Z.Q., Yu, J.B., Ren, Z.M., Deng, K.: Study on the liquid metal flow field in FC-mold of slab continuous casting. Adv. Manuf. **3**(3), 212–220 (2015). DOI 10.1007/s40436-015-0117-2